Journal of Biomechanics 82 (2019) 28–37

Contents lists available at ScienceDirect

Journal of Biomechanics

journal homepage: www.elsevier.com/locate/jbiomech
www.JBiomech.com

Computing the ankle-brachial index with parallel computational fluid dynamics

John Gounley [a], Erik W. Draeger [b], Tomas Oppelstrup [b], William D. Krauss [b], John A. Gunnels [c], Rafeed Chaudhury [d], Priya Nair [d], David Frakes [d], Jane A. Leopold [e], Amanda Randles [a,*]

[a] Department of Biomedical Engineering, Duke University, Durham, NC, USA
[b] Center for Applied Scientific Computing, Lawrence Livermore National Laboratory, Livermore, CA, USA
[c] IBM Research Division, Thomas J. Watson Research Center, Yorktown Heights, NY, USA
[d] Department of Biological and Health Systems Engineering, Arizona State University, Tempe, AZ, USA
[e] Brigham and Women's Hospital, Harvard Medical School, Boston, MA, USA

ARTICLE INFO

Article history:
Accepted 10 October 2018

2010 MSC:
92
76
68

Keywords:
Hemodynamics
Computational fluid dynamics
Ankle-brachial index

ABSTRACT

The ankle-brachial index (ABI), a ratio of arterial blood pressure in the ankles and upper arms, is used to diagnose and monitor circulatory conditions such as coarctation of the aorta and peripheral artery disease. Computational simulations of the ABI can potentially determine the parameters that produce an ABI indicative of ischemia or other abnormalities in blood flow. However, 0- and 1-D computational methods are limited in describing a 3-D patient-derived geometry. Thus, we present a massively parallel framework for computational fluid dynamics (CFD) simulations in the full arterial system. Using the lattice Boltzmann method to solve the Navier–Stokes equations, we employ highly parallelized and scalable methods to generate the simulation domain and efficiently distribute the computational load among processors. For the first time, we compute an ABI with 3-D CFD. In this proof-of-concept study, we investigate the dependence of ABI on the presence of stenoses, or narrowed regions of the arteries, by directly modifying the arterial geometry. As a result, our framework enables the computation a hemodynamic factor characterizing flow at the scale of the full arterial system, in a manner that is extensible to patient-specific imaging data and holds potential for treatment planning.

1. Introduction

Over the last several decades, researchers have used medical image-based hemodynamic simulations as a means to gain insight into the localization and progression of vascular disease (e.g., Taylor et al., 2013; Vergallo et al., 2014). In circulatory conditions such as coarctation of the aorta (CoA) and peripheral artery disease (PAD), blood flow from the heart to the extremities is reduced by a narrowing in the aorta or peripheral arteries, respectively. One standard non-invasive test to screen and monitor patients with CoA and PAD is the ankle-brachial index (ABI), measured as the ratio of the blood pressure in the ankles and arms (Engvall et al., 1995; Warnes et al., 2008; Thani et al., 2011; Aboyans et al., 2012). Systemic arterial flow simulations that compute the ABI have the potential to improve the ability of clinicians to identify, treat, and monitor at-risk patients with circulatory conditions such as CoA and PAD. Simulations could be used to investigate the influence of specific aspects of the vasculature and flow conditions that cannot easily be assessed *in vivo*, such as how an ensemble of lesions collectively influence ABI. Further, hemodynamic models based on patient imaging data have the potential to add insight to treatment planning and incorporate other co-existing conditions (e.g., anemia). In this study, we present a proof-of-concept study to demonstrate the feasibility of computing an ABI using computational fluid dynamics (CFD) simulations in the arterial system.

Existing computational methods for ABI are currently limited to reduced-order 0- and 1-D models (Liang et al., 2009; Li et al., 2013; Pieniak and Cieślicki, 2014; Xiao et al., 2016). The arterial system is divided into a series of segments, through which the flow is modeled with ordinary differential equations, and coupled with lumped parameter models at the ends of the resulting arterial net-

* Corresponding author.
E-mail addresses: john.gounley@duke.edu (J. Gounley), draeger1@llnl.gov (E.W. Draeger), oppelstrup2@llnl.gov (T. Oppelstrup), liam1@llnl.gov (W.D. Krauss), gunnels@us.ibm.com (J.A. Gunnels), rafeed@asu.edu (R. Chaudhury), pnair3@asu.edu (P. Nair), dfrakes@asu.edu (D. Frakes), jleopold@partners.org (J.A. Leopold), amanda.randles@duke.edu (A. Randles).

https://doi.org/10.1016/j.jbiomech.2018.10.007
0021-9290/

work (Sherwin et al., 2003). However, a 1-D model is restricted in describing 3-D phenomena: for instance, the influence of a stenosis on blood pressure in a single vessel must be assumed from a model, rather than derived from the simulation itself. The patient-specificity of the model is also limited relative to 3-D models. Many vascular lesions, stenoses, or dilatations are asymmetric in diameter and length, which is difficult to capture in reduced-order models. Likewise, large and complex 3-D vascular geometries can be created from a patient's medical imaging data.

The computational demands of 3-D computational fluid dynamics (CFD) simulations of blood flow have historically been too memory intensive and computationally complex to compute an ABI. However, the use of high-performance computing resources and development of new massively parallel simulation frameworks have recently progressed toward solving these limitations. For instance, flow has been simulated in increasingly large sections of the arterial system, such as the coronary arteries (Godenschwager et al., 2013), the cerebral arteries (Grinberg et al., 2011), the aorta-femoral artery (Randles et al., 2015a), and the large arteries (Xiao et al., 2013). Computing an ABI is a further challenge, requiring not only a simulation domain on the scale of the full arterial system, but also a simulation resolution which is sufficiently high to obtain grid independent results. Previous simulations in large arterial geometries have found some hemodynamic factors were not grid independent at resolutions achievable with their frameworks (Xiao et al., 2013). Further, these simulations have generally focused on developing massively parallel frameworks rather than applying simulations at this scale to compute quantities of clinical interest.

In a previous paper, a scalable computational methodology, HARVEY, performed blood flow simulations in the full arterial system at 9 μm resolution (Randles et al., 2015b). In this work, we extend this methodology to compute an ABI with 3-D CFD, demonstrating for the first time that massively parallel simulations can calculate an index describing blood flow in the full arterial system. The highly parallel algorithms in HARVEY have been applied to a complex, realistic arterial system geometry and simulated on a large supercomputer. We perform a proof-of-concept study to demonstrate the efficacy of our framework to compute an ABI value. Despite the geometric complexity of the arterial system, we demonstrate that the simulation resolutions obtained are sufficient to compute an ABI which is effectively grid independent. We compare ABI values from steady and pulsatile inflows, and evaluate the influence of stenoses and other changes in the vascular geometry on ABI.

2. Methods

2.1. Parallel computational fluid dynamics

As this study focuses on larger arteries, blood is modeled as a Newtonian fluid subject to the Navier–Stokes equations (Ku, 1997). CFD simulations are conducted with HARVEY, a massively parallel hemodynamics application which implements the lattice Boltzmann method (LBM) (Randles et al., 2013). In the low Mach number limit, the LBM solves the incompressible Navier–Stokes equations (Chen and Doolen, 1998; Aidun and Clausen, 2010). The LBM algorithm is well-suited for simulations in vasculature, due to efficient scaling and simple treatment of boundary conditions in complex geometries, and has been widely applied in this space (e.g., Krafczyk et al., 1998; Artoli et al., 2006; Harrison et al., 2007; Tang et al., 2015; Revell et al., 2016). Physical properties are set to approximate whole blood, including density (1060 kg/m^3) and dynamic viscosity (3.8cP), and blood vessel walls are assumed to be rigid. A complete description of the implementation of LBM in HARVEY is provided in Section A.1 of the Appendix.

Due to their scale and length, HARVEY simulations in the full arterial system were conducted on Vulcan, a 24,576 node IBM Blue Gene/Q supercomputer at Lawrence Livermore National Laboratory. Parallelized with MPI and OpenMP, HARVEY uses parallel algorithms to perform the grid generation and the load balance as well as the fluid dynamics calculations. A distributed exclusive-or (XOR) setup algorithm is applied to the vascular geometry mesh file to produce the Cartesian grid for lattice Boltzmann, as illustrated in Fig. 1. Subsequently, a bisection load balance algorithm performs the domain decomposition in parallel, distributing work among MPI tasks. Further details of the parallelization are provided in Section A.2 of the Appendix.

The HARVEY application has been validated in large arteries with *in vitro* experiments for flow through a CoA. Equivalent flow parameters were used in simulation and experimental domains generated from a patient-specific aortal geometry. The experimental aortal model was produced with lost-core manufacturing and the flow results were measured with particle image velocimetry. As shown in Fig. 2, good agreement between the experimental and simulation results was observed for flow velocity through the coarctation. The coarctation site and the velocity variable were selected for this test due to the complexity of flow in this region and the fundamental importance of velocity to not only the flow distribution that influences ABI but also to derived quantities such as endothelial shear stress. An extended description of the experimental and validation methodology is given in Section A.3 of the Appendix.

In the arterial system geometry, a single inlet is located at the entrance of the aorta, while outlets are located at the ends of arteries throughout the body. In keeping with the proof-of-concept purpose of this study, we make two significant simplifications in our model regarding the inlet and outlet conditions. As a result of these limitations, the flow distribution and ABI in the subsequent simulations may overstate the influence of vessel geometry.

First, flow is driven by either a steady or pulsatile inflow imposed at the inlet using a parabolic flow profile. While not physiological, a steady inflow is employed because the faster time-convergence to steady-state facilitates the assessment of grid independence. As ABI is a ratio of systolic blood pressures, the variation in pressure over a single cycle was not considered crucial to this calculation. Simulations with a pulsatile waveform, shown in Fig. 3, are also conducted.

Second, all outlets are governed by a uniform pressure boundary condition. More sophisticated open- or closed-loop outlet boundary conditions demonstrate superior accuracy for patient-specific flows (Kung and Taylor, 2011; Pirola et al., 2017). However, tuning outflow conditions for the approximately 200 outlets in the arterial system geometry is beyond the scope of this study. The framework introduced here is nonetheless extensible to coupling with Windkessel-based open-loop or 1D-3D closed-loop schemes.

2.2. Configuring a full body arterial system geometry

The arterial system geometry for this study is based on the Visible Human Project, which include CT and MR images at resolutions as high as 0.33 mm pixel width and 1 mm slice thickness (Ackerman, 1998; The Visible Human Project, 2015). From this data, Segars et al. created a series anatomically variable phantoms (Segars et al., 2010; Segars et al., 2013). Of this series, we select a single arterial system phantom, as depicted in Fig. 4. The resulting geometry includes all arteries with maximum diameters greater than 1 mm, including some as narrow as 300 μm across at their minima. The inlet at the base of the aorta and the 211 outlets throughout the body are extruded outward by 2 mm, which cre-

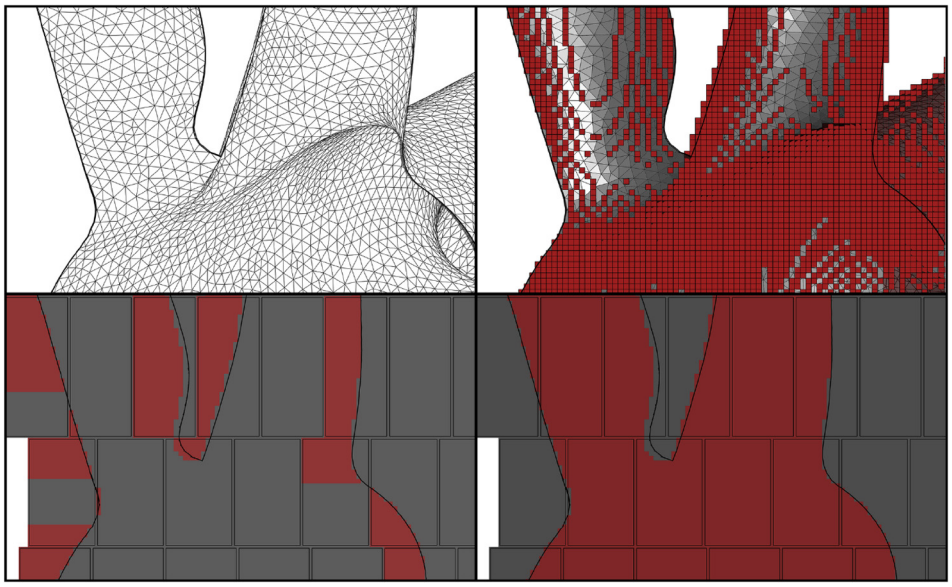

Fig. 1. HARVEY implements an XOR grid set-up algorithm. Starting from the STL file (top left), the red cells (top right) indicate flip points at which the ray passes through the surface. With a simple 3-D domain decomposition, the bottom left figure shows the local calculation of sidedness from the flip points. The bottom right figure shows the resulting calculation of 'insideness' once an exclusive-or operation is applied from left to right. Black lines denote MPI task boundaries and are included to guide the eye. (For interpretation of the references to color in this figure legend, the reader is referred to the web version of this article.)

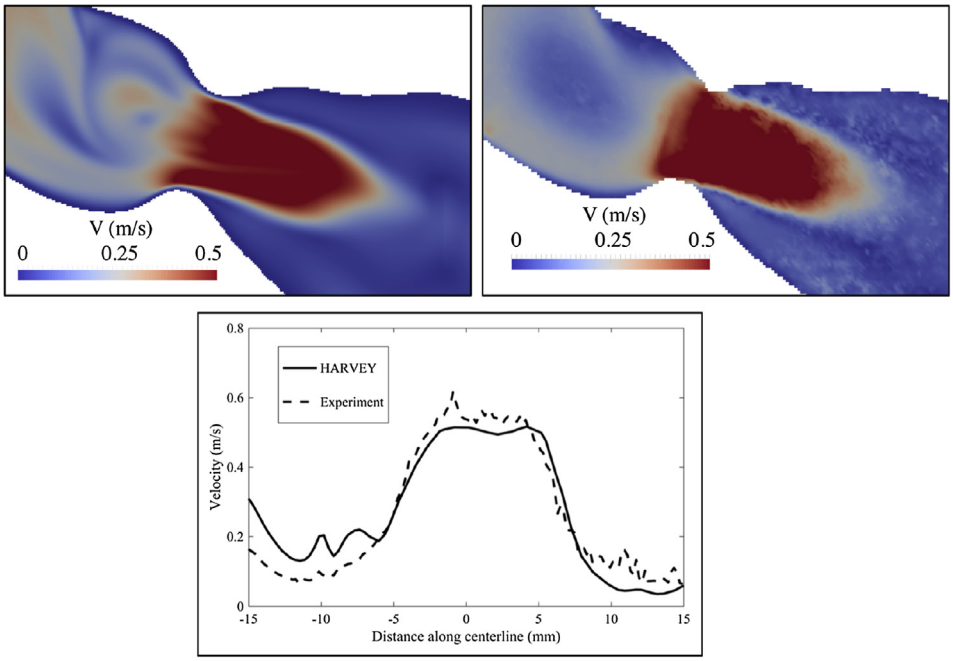

Fig. 2. Flow comparison between experiment (upper left) and computation (upper right) in a CoA for the magnitude of velocity **v**. Below, comparison of velocity along the aorta centerline through the coarctation.

ates a cylindrical channel that facilitates numerical stability in these regions.

ABI measurements *in vivo* are unavailable because the arterial system is not patient-specific. However, this particular geometry has asymmetries well-suited for the computation of ABI on the left and right sides of the body, due to the narrowness of the brachiocephalic artery. The ratio of the left subclavian and brachiocephalic diameters in this geometry is approximately 1.6; this ratio is generally less than 1 in healthy patients (Kahraman et al., 2006). Additionally, the geometry naturally has a 30% stenosis in the brachiocephalic artery. For this and subsequent stenoses, the stenosis percentage is defined as a reduction of the cross-sectional area of the artery by the given percentage in the stenosed region.

2.3. Protocol for computing ABI

Protocols for ABI involve measuring systolic blood pressure in as many as three locations on the left and right sides of the body - the brachial, dorsalis pedis, and posterial tibial arteries. The locations of these arteries are indicated by the numbers 1 – 3, respectively, in Fig. 4. In clinical practice, the highest brachial pressure is

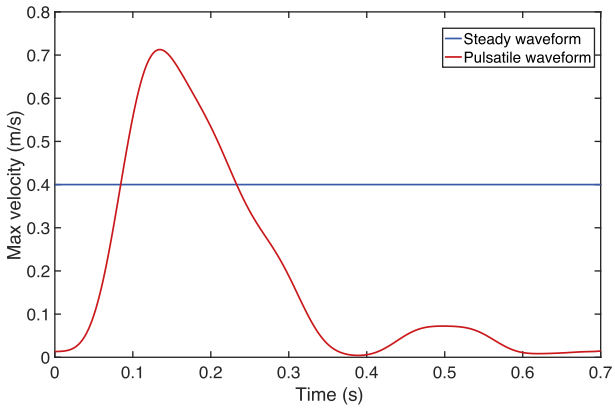

Fig. 3. Maximum velocities for steady and pulsatile waveforms.

combined with a single measurement from each ankle to compute two ABI values. However, in research protocols, values from all six arteries are recorded to provide more comprehensive results (Aboyans et al., 2012).

In HARVEY, pressure is measured in the left and right brachial (P^B), dorsalis pedis (P^{DP}), and posterial tibial (P^{PT}) arteries. Pressure in each artery is computed by averaging over a cross-sectional slice of the vessel. Consistent with research protocol, we use measurements from all three arteries to compute two ABI values for each side:

$$\mathrm{ABI}_{L1} = \frac{P_L^{DP}}{P_L^B} \qquad \mathrm{ABI}_{L2} = \frac{P_L^{PT}}{P_L^B} \tag{1}$$

$$\mathrm{ABI}_{R1} = \frac{P_R^{DP}}{P_R^B} \qquad \mathrm{ABI}_{R2} = \frac{P_R^{PT}}{P_R^B} \tag{2}$$

in which the (L,R) subscript indicates the side of the body and the (1,2) subscript denotes the ankle artery used. ABI values are computed from pressures at the same timepoint in the simulation for steady flow, but from the values at maximum systole of the cardiac cycle for pulsatile flow.

3. Results

3.1. Influence of grid resolution on ABI

The attainment of a resolution at which CFD results are effectively independent of the grid is a necessary prerequisite for accurate simulations. Distinct from validation, a grid independence study demonstrates that simulations are being performed at an appropriate resolution to avoid artifacts of the discretization. To assess the influence of grid resolution on ABI computation, simulations with steady flow are conducted at a range of resolutions from 50 to 200 μm. Due to arterial system complexity, we do not expect to achieve theoretical numerical convergence. Rather, we aim to demonstrate that, beyond a certain threshold, the computed ABI values become effectively independent of grid resolution.

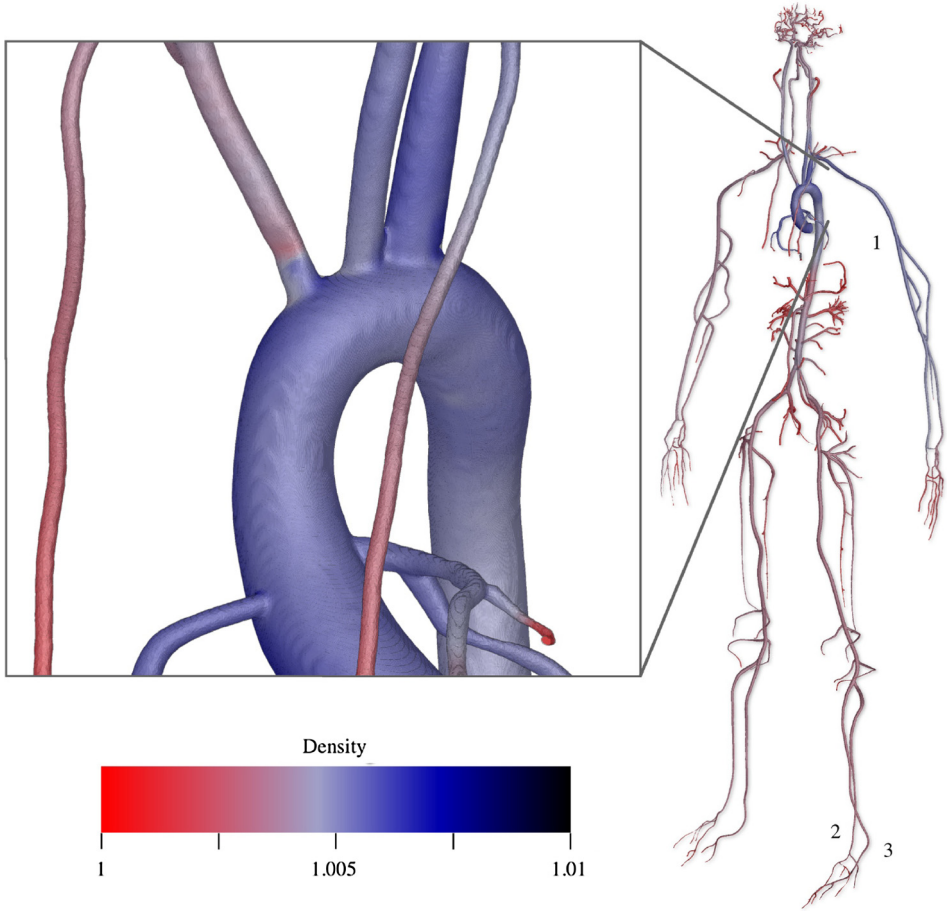

Fig. 4. Image of arterial system geometry, with an inset of the arteries around the aortic arch and colored by simulation results for density ρ. The role of density in computing pressure in LBM is discussed in Section A.1 of the Appendix. (For interpretation of the references to color in this figure legend, the reader is referred to the web version of this article.)

Table 1
Simulation results from steady flow for computed left ABIs, ABI_{L1} and ABI_{L2}, shown at resolutions from 50 to 20 μm. Relative error is the relative difference from ABI computed at 5 μm resolution.

Res. (μm)	MPI Tasks	ABI_{L1}	ABI_{L2}	Rel. Err. ABI_{L1}	Rel. Err. ABI_{L2}
200	512	0.652	0.656	24.9%	22.6%
150	2048	0.598	0.604	14.6%	12.9%
125	32768	0.578	0.587	10.7%	9.7%
100	32768	0.538	0.548	3.1%	2.4%
76	131072	0.535	0.542	2.5%	1.3%
60	262144	0.533	0.539	2.1%	0.8%
50	393216	0.522	0.535	–	–

The influence of grid resolution is evaluated in Table 1 by considering the computed left ABIs. ABI measurements using either left ankle artery agree well over the range of resolutions considered, deviating by 0.013 or less. Relative error at each grid resolution is computed with respect to the ABI measurement at 50 μm. This relative error decreases monotonically with increased grid resolution. As anticipated, we do not observe theoretical numerical convergence within the range of resolutions considered.

The ABI measurements become reasonably consistent at 100 μm, varying by 3% or less from the value at 50 μm. This consistency contrasts sharply with results at 125 μm, at which relative error was still approximately 10%. Apparently, for the minimum arterial diameter included in this arterial system geometry, a threshold near 100 μm resolution exists for reliable ABI computation. Particularly near outlets, some arteries in the geometry are as narrow as 300 μm and locally significant changes in the simulation domain occur in these regions as the resolution is increased. It is somewhat surprising, therefore, that we find ABI measurements to be independent of grid resolution beyond 100 μm resolution.

By comparison, different severities of PAD involve ABI classification regions of 0.2 or more, corresponding to roughly 20% of a healthy ABI ≈ 1. In this context, the 3% error observed at 10 μm seems acceptable. Although still large, the simulation scale for a 10 μm resolution is remarkably tractable when compared with cellular-level resolutions used in previous simulations of the full arterial system (Randles et al., 2015b).

3.2. Steady vs. pulsatile flow

The steady flow case is not without clinical relevance (e.g., left ventricular assist devices and ECMO devices) or potential computational advantage (i.e., steady-state Navier–Stokes solvers). Nonetheless, simulation fidelity for most applications generally requires pulsatile inflows which approximate the cardiac cycle. Computing an ABI with a pulsatile inflow potentially presents an additional challenge, as several cycles must be simulated before attaining a periodic steady-state. In this section, we assess the time-convergence of ABI in a pulsatile flow and compare the ABI values from steady and pulsatile flows.

To assess time-convergence of ABI, three cycles of the pulsatile waveform from Fig. 3 are simulated. Based on the previous section, simulations are conducted at 10 μm resolution. Relative error is computed between the ABI values measured in the first and second cycles, relative to the third cycle. As shown in Table 2, ABI values computed in the second and third cycles are virtually identical. Even in the first cycle, with the flow initially quiescent, the relative error is still very reasonable. In contrast, simulations in aortal geometries with more complex outlet conditions are reported to require $4-6$ cycles to produce periodic flow results (LaDisa et al., 2011).

Table 2
Time convergence of ABI for successive cycle of pulsatile flow. Relative error is the relative difference from ABI computed in the 3rd cycle.

ABI	Rel. Err. Cycle 1	Rel. Err. Cycle 2
ABI_{L1}	2.8%	0.3%
ABI_{R1}	1.9%	0.0%
ABI_{L2}	2.4%	0.2%
ABI_{R2}	2.2%	0.0%

In Fig. 5, pulsatile ABI values from the third cardiac cycle are compare with steady inflow ABIs. To the extent that geometry determines flow distribution, one might expect ABI values for steady and pulsatile inflows to be broadly similar. This is borne out in the results, as right ABIs exceed left ABIs for both inflow patterns. Of course, in the absence of a patient-specific geometry and clinical measurements, we cannot hypothesize about which inflow pattern is more accurate. For more complex outflow conditions, we would expect a significant deviation between ABIs from steady and pulsatile ABIs. However, in the simplified setting for this study, it appears that steady inflow is sufficient to compute a meaningful ABI and, as a result, such flows will be employed in the subsequent section.

3.3. Influence of vessel diameter and stenoses on ABI

We perform CFD simulations to better illustrate the efficacy of our framework to measure the influence of stenoses and other geometric changes on the current arterial system. We focus on two settings, the brachiocephalic artery and the descending aorta, that address the left/right and ankle/brachial aspects of ABI, respectively. Four additional arterial system geometries are created with the mesh editing software Meshmixer, as illustrated in the top left of Fig. 6. In the first geometry, we enlarge the brachiocephalic artery so that the diameter is approximately equal to the left subclavian. In the remaining three geometries, we introduce coarctations in the descending aorta: a single 60% coarctation, a single 80% aortic coarctation, and two 60% aortic coarctations in series. Based on the grid independence study in Section 3.1, we conduct

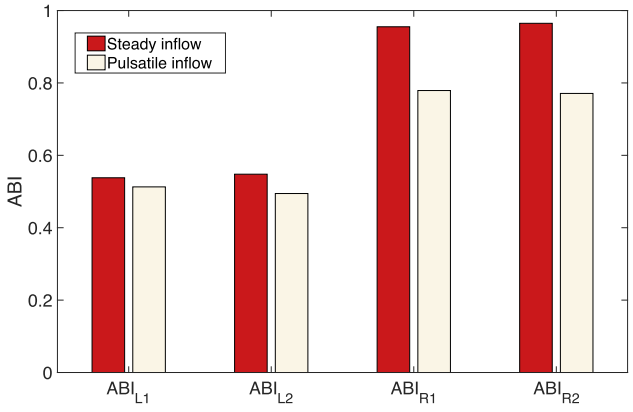

Fig. 5. Comparison of ABI values for steady and pulsatile inflows.

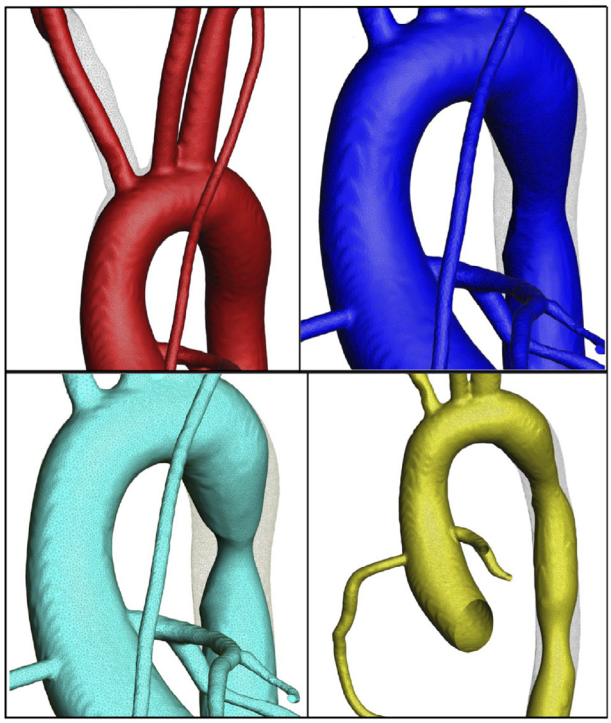

Fig. 6. In top left, original arterial system (red) versus arterial system with enlarged brachiocephalic artery (gray). In remaining images, original arterial system (gray) compared with arterial systems with a 60% aortal coarctation (blue, top right), 80% aortal coarctation (teal, bottom left), and two 60% aortal coarctations in series (gold, bottom right). To emphasize the regions where the arterial geometry was modified, not all vessels are shown in these images. (For interpretation of the references to color in this figure legend, the reader is referred to the web version of this article.)

steady flow simulations at 10 μm resolution in each additional arterial system. Results for the four ABI values in each arterial systems are presented in Fig. 7.

A stenosis in the arteries supplying blood to a single side of the body can cause significantly different left and right ABI values. In the original arterial system, we observe a low ABI (≈ 0.53) on the left, but a more normal right ABI (≈ 0.96). We hypothesize that the primary cause of this difference is the narrowness of the brachiocephalic artery relative to the left subclavian artery. Like a right subclavian stenosis, this narrowness may lead to a lower left than right ABI (Shadman et al., 2004; Aboyans et al., 2012). This effect may be exacerbated by the outflow conditions in the simulation, which do not account for different downstream resistances at each outlet. To assess this hypothesis, we compare the ABI values from the arterial system with the enlarged brachiocephalic artery. As expected, simulations show increased flow to the right arm and produce similar left $(0.53 - 0.54)$ and right $(0.57 - 0.58)$ ABI values.

Conversely, a coarctation in the descending aorta is expected to symmetrically decrease left and right ABIs (Raimundo and Machado, 2012). To test the ability of the computational model to reproduce the expected changes, we compare ABI values from the three geometries with aortic coarctations with the original geometry. Results show an approximately symmetric change in left and right ABIs: 16 & 20% decreases for the 60% coarctation, 33 & 35% for the two 60%s in series, and 54 & 61% for the 80%. Clinical tests typically focus on ABI for a single stenosis, but additional stenoses elsewhere may obscure the relative role of the single stenosis in determining ABI (Guo et al., 2007). In our simulations, the decrease in ABI for two 60% coarctations in the descending aorta is roughly twice the decrease for a single 60% coarctation, consistent with the intuitive conclusion that the influence of multiple stenoses on ABI within a single blood vessel is cumulative. Further, analysis of *in vivo* ABI data has indicated that ABI has a higher sensitivity for severe stenoses (Xu et al., 2010). The model of Li *et al.* showed similar results for stenoses in several leg and arm arteries (Li et al., 2013). Our simulations are consistent with this trend, as the 80% coarctation causes a much larger decrease than even two 60% coarctations.

4. Discussion

Although previous studies have computed ABI with reduced-order models, 3-D CFD simulations constitute a significant improvement by enabling the use of vascular geometries derived from imaging data. Imaging data allows the model to incorporate factors like 3-D vessel shape that cannot be fully represented in reduced-order models. The influence of vessel geometry on blood pressure has been clearly shown, for instance, on patients with a surgically repaired CoA (Ou et al., 2004; Ou et al., 2008). Likewise, the strong association of endothelial shear stress with atherosclerosis suggests the value of computing local hemodynamic factors in combination with ABI (Chatzizisis et al., 2007; Brevetti et al.,

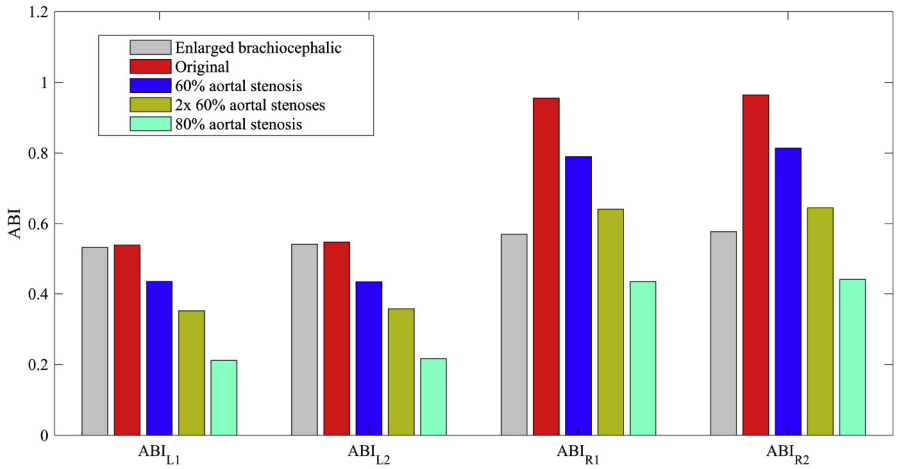

Fig. 7. Left and right ABI for arterial systems with, from left to right, an enlarged brachiocephalic artery (gray), the original arterial system (red), a single 60% aortic coarctation (blue), two 60% aortic coarctations in series (gold), and a single 80% aortic coarctation (teal). (For interpretation of the references to color in this figure legend, the reader is referred to the web version of this article.)

2008). Another advantage of the 3-D model is incorporation of vascular abnormalities which may be concomitant with CoA or PAD. This includes not only stenoses located outside of the region of interest but also co-existing conditions, such as the heightened prevalence of intercranial aneurysms among adult CoA patients (Bhatt et al., 2015). In sum, 3-D CFD simulations over the arterial system present two major advantages for computing ABI: improved fidelity by fully representing the complexity of 3-D vessel geometries and a more comprehensive view of both primary and concomitant circulatory conditions. These advantages have the potential to balance the additional effort required for patient imaging and increased computational cost.

Nonetheless, there is also significant potential for computing ABI with coupled 3-D and reduced order models. Recently reviewed by (Quarteroni et al., 2016), this coupling could take multiple forms. First, a natural extension of the 3-D framework introduced in this study is the incorporation of a lumped-parameter model, such as a Windkessel-based scheme, to define unique outflow conditions for each outlet. Second, a broader coupling scheme could employ 3-D CFD for specific regions of interest but use a reduced-order model for the remaining vasculature. For conditions that can be well-localized, the latter approach offers the potential to reduce effort but retain some of the advantages of 3-D CFD. Instead, the added computational expense of 3-D simulations can be targeted toward only vascular regions of especial interest.

Large scale CFD simulations of ABI have the potential to improve clinical care of patients with CoA and PAD. Individual arteries or the entire arterial system from patient-specific imaging data can be used to compute a patient-specific ABI. The usage of imaging data from a specific patient would allow clinicians to identify arteries requiring treatment for PAD or to assess how a potential treatment for CoA might improve systemic circulation. In future work, we aim to validate this 3-D CFD framework with patient-specific *in vivo* ABI measurements and investigate the association of ABI with other risk factors such as endothelial shear stress and local pressure gradients. Our long-term goal is to develop a robust, patient-specific tool for both diagnostic tests and personalized treatment planning.

5. Conclusion

We have developed a scalable computational framework for simulating blood flow in vascular geometries. Because the algorithms used for generation of the 3-D simulation domain, for balancing the computational load, and for performing the flow simulation are highly parallelized and scalable, simulations with this framework may be conducted on large supercomputers. This computational performance allows for hemodynamic simulations to be conducted on large portions of the vasculature and at high resolutions. This capability enables computation of a clinical diagnostic indicator, ABI, that characterizes the flow of blood in the full arterial system.

Conflict of interest statement

None declared.

Acknowledgments

We thank Don Frederick and the Livermore Computing Operations team at Lawrence Livermore National Laboratory (LLNL) for helping with the full system runs on Vulcan. This work was performed under the auspices of the U.S. Department of Energy by LLNL under Contract DE-AC52-07NA27344. Computing support for this work came from the LLNL Institutional Computing Grand Challenge program. Support was also provided by the LLNL Laboratory Directed Research and Development (LDRD) program.

Research reported in this publication was supported by the Office of the Director, National Institutes of Health under Award Number DP5OD019876. The content is solely the responsibility of the authors and does not necessarily represent the official views of the National Institutes of Health. This material is based upon work supported by the National Science Foundation under Grant No. 1512553. Support was provided by the Big Data-Scientist Training Enhancement Program (BD-STEP) of the Department of Veterans Affairs.

Appendix A

A.1. Lattice Boltzmann method

HARVEY is a massively parallel hemodynamics application which implements the lattice Boltzmann method (Randles et al., 2013). Based on the Boltzmann equation of kinetic theory, lattice Boltzmann represents the flow as a probability distribution function f of particles moving about a fixed Cartesian lattice at discrete velocities (He and Luo, 1997; Chen and Doolen, 1998). For the D3Q19 discretization of 3-D velocity space used in HARVEY, the distribution f has 19 components f_i, with the velocity $\mathbf{c}_i$ at each lattice point $\mathbf{x}$. The time evolution of f is governed by the lattice Boltzmann equation,

$$f_i(\mathbf{x}+\mathbf{c}_i, t+1) = f_i(\mathbf{x}, t) - \Omega\left(f_i(\mathbf{x}, t) - f_i^{eq}(\mathbf{x}, t)\right) + F_i, \tag{A.1}$$

for collision kernel Ω, and Maxwell–Boltzmann equilibrium distribution f_i^{eq}, and external force distribution F. The influence of the gravitational force $\mathbf{G}$ on flow is incorporated into Eq. (A.1) by the methods of Buick (2000) and Guo et al. (2002). First, fluid density ρ and velocity $\mathbf{u}$ are computed as moments of f with the equations:

$$\rho = \sum_i f_i \qquad \rho\mathbf{u} = \sum_i \mathbf{c}_i f_i + \frac{1}{2}\mathbf{G} \tag{A.2}$$

Second, the gravitational force $\mathbf{G}$ is converted into external force distribution F by the relation

$$F_i = \left(1 - \frac{1}{2\tau}\right)\omega_i \left[\frac{\mathbf{c}_i - \mathbf{u}}{c_s^2} + \frac{\mathbf{c}_i \cdot \mathbf{u}}{c_s^4}\mathbf{c}_i\right] \cdot \mathbf{G} \tag{A.3}$$

for the lattice speed of sound $c_s = 1/\sqrt{3}$. Finally, the Maxwell–Boltzmann equilibrium distribution is defined as

$$f_i^{eq}(\mathbf{x}, t) = \omega_i \rho \left(1 + \frac{\mathbf{c}_i \cdot \mathbf{u}}{c_s^2} + \frac{\mathbf{u}\mathbf{u} : (\mathbf{c}_i\mathbf{c}_i - c_s^2\mathbf{I})}{2c_s^4}\right) \tag{A.4}$$

for weights ω_i. HARVEY uses the single relaxation time Bhatnagar-Gross-Krook (BGK) collision kernel $\Omega = \frac{1}{\tau}$. The non-dimensional relaxation time τ is based on kinematic fluid viscosity $\nu = c_s^2(\tau - \frac{1}{2})$.

In LBM, total pressure is related to density by an equation of state based on the ideal gas law (Krüger et al., 2017). Gauge (blood) pressure p is extracted using the relation $p = c_s^2(\rho - \rho_{\text{atm}})$, in which the reference parameter ρ_{atm} is set separately for steady and pulsatile flows. The standard conversion of physical parameters to and from lattice Boltzmann space is employed (Junk and Kehrwald, 2006).

Two types of boundary conditions are employed in the model. First, the artery walls are assumed to be rigid and governed by a no-slip boundary condition using the halfway bounce-back method (Ziegler, 1993). Second, the open boundary conditions at the inlets and outlets of the blood vessels are implemented with a finite-difference velocity gradient method (Latt et al., 2008).

A.2. Parallel implementation

In HARVEY, the lattice Boltzmann algorithm is implemented in C and C++ and is fully parallelized with MPI and OpenMP (Randles et al., 2013). A 1-lattice point-wide halo surrounds the bounding box of lattice points belonging to each task. During preprocessing, communication tables are computed between neighboring tasks with overlapping halos and data within these halo regions are exchanged at each iteration using non-blocking MPI calls. No global communication between tasks is required. On the IBM Blue Gene/Q system, HARVEY scales efficiently up to 1.6 million cores (Randles et al., 2015a; Randles et al., 2015b). The size and scale of simulating the full arterial system present challenges related to data structure, lattice generation, and load balance.

A.2.1. Data structure

For the full arterial system, the simulation domain accounts for approximately 0.16% of the bounding box around the geometry. To limit the required memory capacity, lattice points are addressed with an indirect scheme (Schulz et al., 2002). With indirect addressing, only the lattice points corresponding to the fluid domain and inner vessel wall are stored. Although indirect addressing dramatically reduces the number of lattice points stored in memory, it complicates the lattice Boltzmann algorithm because the locations of neighboring lattice points in memory are not known implicitly. To mitigate this effect, we exploit the stencil organization to create and store an adjacent list containing the required information about neighboring lattice points for the lattice Boltzmann algorithm during preprocessing.

A.2.2. Lattice generation

The full arterial system geometry is stored as a triangulated surface mesh in stereolithography (STL) format. At runtime, HARVEY generates a regular Cartesian lattice of the desired resolution by determining the grid points that lie within the interior of the surface mesh. There are numerous algorithms for computing the points inside a closed surface, such as the use of angle-weighted pseudonormals (Baerentzen and Aanaes, 2005) to compute the shell of grid points just inside the surface mesh. These shell points can then be connected along lattice axes to form the complete interior volume grid. However, while a parallel implementation of this approach has been used successfully by HARVEY on large arterial systems (Randles et al., 2015a), it was fundamentally memory-constrained, as the construction of the interior volume grid from shell points requires a task to temporarily own all grid points spanning one or more box dimensions. This memory constraint is further exacerbated by the challenge of choosing an initial domain decomposition that is not severely load imbalanced. To enable the large, high-resolution simulations of the full arterial network needed to compute ABI, it was necessary to develop a new highly-distributed parallel algorithm to compute the volume grid from a surface mesh without ever collecting global information.

The first step is to distribute the surface mesh triangles equally across all tasks. For each triangle, we need to compute the intersection points along a chosen Cartesian axis (in this case, the x-axis) of any rays along that axis that lie on grid points. This computation is most simply done by computing the 2-D bounding box of the triangle in the yz-plane in grid coordinates and using integer operations to find all possible grid points whose rays could potentially intersect. The Möller-Trumbore intersection algorithm (Möller and Trumbore, 1997) is then used on each ray to determine whether it intersects with a triangle. If so, the intersection coordinate is computed and stored. The set of these coordinates, the 'flip points', defines every point at which a ray sweeping from one side of the box to the other will move from outside-to-inside the surface mesh or the converse. A simple 3-D domain decomposition is then computed using planar bounding boxes to determine the maximum possible enclosed volume of each yz-plane and assigning roughly equal volume to each task. Flip points are then redistributed so that each task owns all points within its bounding box.

Within each task's domain, the 'insideness' is temporarily stored as a single bit and initially set to false. For each local flip point, the insideness of all grid points to the right of the flip point in the x-direction is toggled. This is illustrated in the center panel of Fig. 1. At this point, tasks whose bounding box lie entirely inside the surface mesh are indistinguishable from tasks that lie entirely outside, as neither task owns any flip points, thus, their insideness array is entirely false. The final step is to carry out an exclusive-or (XOR) at the boundaries, moving from left to right, as shown in the bottom right panel of Fig. 1. This step propagates the boundary information across the entire box while requiring only nearest-neighbor communication of a single scalar per boundary point. Now each task can compute all interior and boundary points within its bounding box and supply this information to the load balancer.

A.2.3. Load balance

Effective load balance is a critical component of efficient parallel computation of large arterial systems. As with the lattice generation, however, it can be challenging to load balance these systems effectively without exceeding the local memory. To avoid exceeding the local memory, we use an efficient recursive bisection algorithm designed to distribute the work into increasingly smaller pieces using a weighted cost function. At each level of bisection, the longest dimension of the subdomain is binned and a histogram of the cost function is computed by summing the contributions in each bin. A cut point is chosen that divides the work as evenly as possible, and halves the subdomain's tasks assigned to each side. The load is redistributed using efficient point-to-point communication routines and the process is repeated until each subdomain consists of only one task. Each level of recursion requires only the tasks in the subdomain and can thus be performed simultaneously.

This approach is both fast and lightweight, making it possible to dynamically recompute load balance as needed throughout a simulation. The primary challenge is defining a cost function that accurately captures the real work load of interacting domains, as only the cost of fluid and boundary nodes owned by a given task is reflected in the function. As the number of parallel tasks increases, the ratio of owned nodes to ghost nodes decreases and this cost function becomes less accurate. We are exploring modifications to the algorithm that can compensate for such surface effects by adding additional weight to the costs of particles on bisection boundaries throughout the recursion. It is also necessary to include a small volume term to the cost function to prevent the algorithm from creating tasks with large bounding boxes that span multiple arterial branches, as this creates inefficiencies in both memory usage and communication.

A.3. Validation with in vitro experiment

For the purpose of validating the computational algorithm for flow in larger arteries, we performed a direct comparison of HARVEY with an *in vitro* flow measured experimentally with particle image velocimetry (PIV). A patient-specific aortal geometry that included a significant CoA was obtained from the Open Source Medical Software Corporation repository (Wilson et al., 2013). An optically clear aorta model was constructed from this geometry using a lost-core manufacturing technique (Nair et al., 2016).

Experiments were conducted in a flow loop consisting of (1) a custom piston pump, (2) the optically clear urethane model (PolyOptic 1411 ES7, Polytek, Easton, PA) of the aorta, and (3) a reservoir

filled with blood analog solution (Chaudhury et al., 2015; Chaudhury et al., 2016). Connected to the flow loop with felxible Tygon tubing (R-3603, Ryan Herco Flow Solutions, Burbank, CA), the aorta model was staged for optical imaging such that a laser light sheet passed through the center-plane of the coarctation. Sodium iodide-based solution was used as the blood analog, with refractive index matching the urethane block (n = 1.49). This eliminated optical distortion during PIV by rendering the urethane wall invisible. In the aorta model, PIV was used to measure the velocity field on a plane which passed lengthwise along the coarctation. Further details about the PIV technique and parameters are found in our previous work (Gounley et al., 2016).

Equivalent fluid, inflow, and outflow parameters were used for the *in vitro* experiment and HARVEY simulation: kinematic fluid viscosity $\nu = 2.05\ \mathrm{m^2/s}$, fluid density $\rho = 1750\ \mathrm{kg/m^3}$, and a volumetric flow rate at the inlet equivalent to a Poiseuille flow profile with a maximum velocity of 0.4 m/s. A free surface condition governed the outlets in the experiment, comparable to the pressure boundary condition used at the outlets in the simulation. HARVEY simulations were conducted at 100 μm resolution, whereas PIV data are shown at 200 μm resolution.

A direct comparison between experiment and simulation is conducted for flow velocity through a lengthwise slice of the coarctation. Fig. 2 shows results of only a small portion of the larger simulation and experiment. In these images, fluid flows down through a coarctation in the descending aorta from top left to bottom right. Despite unavoidable minor differences in the geometries, the qualitative aspects of the flow profile through the coarctation clearly match. Compared with the experimental results, the computational simulations do show somewhat more recirculation and transverse flow above the coarctation. Nonetheless, for the velocity at the vessel centerline, we observe consistent agreement between the HARVEY simulation and experiment over the entire region of the geometry considered. This comparison demonstrates the validity of the numerical methodology in HARVEY for simulating steady flow in large vascular geometries.

References

Aboyans, V., Criqui, M.H., Abraham, P., Allison, M.A., Creager, M.A., Diehm, C., Fowkes, F.G.R., Hiatt, F.G.R., Lacroix, W.R., Jönsson, B., Lacroix, P., et al., 2012. Measurement and interpretation of the ankle-brachial index: A scientific statement from the American Heart Association. Circulation 126 (24), 2890–2909.

Ackerman, M.J., 1998. The Visible Human Project. Proc. IEEE 86 (3), 504–511.

Aidun, C.K., Clausen, J.R., 2010. Lattice-boltzmann method for complex flows. Ann. Rev. Fluid Mech. 42, 439–472.

Artoli, A.M., Hoekstra, A.G., Sloot, P.M., 2006. Mesoscopic simulations of systolic flow in the human abdominal aorta. J. Biomech. 39 (5), 873–884.

Baerentzen, J., Aanaes, H., 2005. Signed distance computation using the angle weighted pseudonormal. IEEE Trans. Vis. Comput. Graph. 11 (3), 243–253.

Bhatt, A.B., Foster, E., Kuehl, K., Alpert, J., Brabeck, S., Crumb, S., Davidson, W.R., Earing, M.G., Ghoshhajra, B.B., Karamlou, T., et al., 2015. Congenital heart disease in the older adult: a scientific statement from the american heart association. Circulation 131 (21), 1884–1931.

Brevetti, G., Schiano, V., Chiariello, M., 2008. Endothelial dysfunction: a key to the pathophysiology and natural history of peripheral arterial disease? Atherosclerosis 197 (1), 1–11.

Buick, J., 2000. Gravity in a lattice Boltzmann model. Phys. Rev. E 61 (5), 5307.

Chatzizisis, Y.S., Coskun, A.U., Jonas, M., Edelman, E.R., Feldman, C.L., Stone, P.H., 2007. Role of endothelial shear stress in the natural history of coronary atherosclerosis and vascular remodeling: molecular, cellular, and vascular behavior. J. Am. Coll. Cardiol. 49 (25), 2379–2393.

Chaudhury, R.A., Herrmann, M., Frakes, D.H., Adrian, R.J., 2015. Length and time for development of laminar flow in tubes following a step increase of volume flux. Exp. Fluids 56 (1). 22-10.

Chaudhury, R.A., Atlasman, V., Pathangey, G., Pracht, N., Adrian, R.J., Frakes, D.H., 2016. A high performance pulsatile pump for aortic flow experiments in 3-dimensional models. Cardiovasc Eng. Technol. 7 (2), 148–158.

Chen, S., Doolen, G.D., 1998. Lattice Boltzmann method for fluid flows. Ann. Rev. Fluid Mech. 30 (1), 329–364.

Engvall, J., Sonnhag, C., Nylander, E., Stenport, G., Karlsson, E., Wranne, B., 1995. Arm-ankle systolic blood pressure difference at rest and after exercise in the assessment of aortic coarctation. Heart 73 (3), 270–276.

Godenschwager, C., Schornbaum, F., Bauer, M., Köstler, H., Rüde, U., 2013. A framework for hybrid parallel flow simulations with a trillion cells in complex geometries. In Proc. Proc. International Conference for High Performance Computing, Networking, Storage and Analysis. ACM, p. 35.

Gounley, J., Chaudhury, R., Vardhan, M., Driscoll, M., Pathangey, G., Winarta, K., Ryan, J., Frakes, D., Randles, A., 2016. Does the degree of coarctation of the aorta influence wall shear stress focal heterogeneity? In: Conf. Proc. IEEE Eng. Med. Biol. Soc.. IEEE, pp. 3429–3432.

Grinberg, L., Insley, J.A., Morozov, V., Papka, M.E., Karniadakis, G.E., Fedosov, D., Kumaran, K., 2011. A new computational paradigm in multiscale simulations: Application to brain blood flow. In: Proc. International Conference for High Performance Computing, Networking, Storage and Analysis. IEEE, pp. 1–12.

Guo, Z., Zheng, C., Shi, B., 2002. Discrete lattice effects on the forcing term in the lattice Boltzmann method. Phys. Rev. E 65 (4), 046308.

Guo, X., Li, J., Pang, W., Zhao, M., Luo, Y., Sun, Y., Hu, D., 2007. Sensitivity and specificity of ankle-brachial index for detecting angiographic stenosis of peripheral arteries. Circulation 72 (4), 605–610.

Harrison, S., Smith, S., Bernsdorf, J., Hose, D., Lawford, P., 2007. Application and validation of the lattice Boltzmann method for modelling flow-related clotting. J. Biomech. 40 (13), 3023–3028.

He, X., Luo, L.-S., 1997. Theory of the lattice Boltzmann method: From the Boltzmann equation to the lattice Boltzmann equation. Phys. Rev. E 56 (6), 6811.

Junk, M., Kehrwald, D., 2006. On the relation between lattice variables and physical quantities in lattice Boltzmann simulations. ITWM Report.

Kahraman, H., Ozaydin, M., Varol, E., Aslan, S.M., Dogan, A., Altinbas, A., Demir, M., Gedikli, O., Acar, G., Ergene, O., 2006. The diameters of the aorta and its major branches in patients with isolated coronary artery ectasia. Tex. Heart I J. 33 (4), 463.

Krafczyk, M., Cerrolaza, M., Schulz, M., Rank, E.., 1998. Analysis of 3d transient blood flow passing through an artificial aortic valve by lattice–Boltzmann methods. J. Biomech. 31 (5), 453–462.

Krüger, T., Kusumaatmaja, H., Kuzmin, A., Shardt, O., Silva, G., Viggen, E.M., 2017. The Lattice Boltzmann Method. Springer.

Ku, D.N., 1997. Blood flow in arteries. Ann. Rev. Fluid Mech. 29 (1), 399–434.

Kung, E.O., Taylor, C.A., 2011. Development of a physical Windkessel module to re-create in vivo vascular flow impedance for in vitro experiments. Cardiovasc. Eng. Technol. 2 (1), 2–14.

LaDisa, J.F., Figueroa, C.A., Vignon-Clementel, I.E., Kim, H.J., Xiao, N., Ellwein, L.M., Chan, F.P., Feinstein, J.A., Taylor, C.A., et al., 2011. Computational simulations for aortic coarctation: representative results from a sampling of patients. J. Biomech. Eng. 133 (9), 091008.

Latt, J., Chopard, B., Malaspinas, O., Deville, M., Michler, A., 2008. Straight velocity boundaries in the lattice Boltzmann method. Phys. Rev. E. 77 (5), 056703.

Liang, F., Takagi, S., Himeno, R., Liu, H., 2009. Multi-scale modeling of the human cardiovascular system with applications to aortic valvular and arterial stenoses. Med. Biol. Eng. Comput. 47 (7), 743–755.

Li, X., Wang, L., Zhang, C., Li, S., Pu, F., Fan, Y., Li, D., 2013. Why is ABI effective in detecting vascular stenosis? Investigation based on multibranch hemodynamic model. Sci. World J.

Möller, T., Trumbore, B., 1997. Fast, minimum storage ray/triangle intersection. J. Graphics Tools 2 (1), 21–28.

Nair, P., Chong, B.W., Indahlastari, A., Ryan, J., Workman, C., Babiker, M.H., Farsani, H.Y., Baccin, C.E., Frakes, D., 2016. Hemodynamic characterization of geometric cerebral aneurysm templates treated with embolic coils. J. Biomech. Eng. 138 (2), 021011.

Ou, P., Bonnet, D., Auriacombe, L., Pedroni, E., Balleux, F., Sidi, D., Mousseaux, E., 2004. Late systemic hypertension and aortic arch geometry after successful repair of coarctation of the aorta. Eur. Heart J. 25 (20), 1853–1859.

Ou, P., Celermajer, D.S., Raisky, O., Jolivet, O., Buyens, F., Herment, A., Sidi, D., Bonnet, D., Mousseaux, E., 2008. Angular (gothic) aortic arch leads to enhanced systolic wave reflection, central aortic stiffness, and increased left ventricular mass late after aortic coarctation repair: evaluation with magnetic resonance flow mapping. J. Thorac. Cardiovasc. Surg. 135 (1), 62–68.

Pieniak, M., Cieślicki, K., 2014. Properties of ankle-brachial-index (ABI) in the light of numerical simulation of pulse wave propagation. In: Mechatronics 2013. Springer, pp. 809–815.

Pirola, S., Cheng, Z., Jarral, O., O'Regan, D., Pepper, J., Athanasiou, T., Xu, X., 2017. On the choice of outlet boundary conditions for patient-specific analysis of aortic flow using computational fluid dynamics. J. Biomech. 60, 15–21.

Quarteroni, A., Veneziani, A., Vergara, C., 2016. Geometric multiscale modeling of the cardiovascular system, between theory and practice. Comput. Methods Appl. Mech. Eng. 302, 193–252.

Raimundo, M., Machado, A.P., 2012. Aortic coarctation misdiagnosed as a descending thoracic aorta aneurysm. Rev. Port. Cardiol. 31 (5), 381–384.

Randles, A.P., Kale, V., Hammond, J., Gropp, W., Kaxiras, E., 2013. Performance analysis of the lattice Boltzmann model beyond Navier-Stokes. In: Parallel & Distributed Processing (IPDPS), 2013 IEEE 27th International Symposium on. IEEE, pp. 1063–1074.

Randles, A., Draeger, E.W., Bailey, P.E., 2015a. Massively parallel simulations of hemodynamics in the primary large arteries of the human vasculature. J. Comp. Sci. 9, 70–75.

Randles, A., Draeger, E.W., Oppelstrup, T., Krauss, L., Gunnels, J.A., 2015b. Massively parallel models of the human circulatory system. In: Proc International Conference for High Performance Computing, Networking, Storage and Analysis. ACM, p. 1.

Revell, A., Mandal, P., Day, P., et al., 2016. Application of a lattice Boltzmann-immersed boundary method for fluid-filament dynamics and flow sensing. J. Biomech. 49 (11), 2143–2151.

Schulz, M., Krafczyk, M., Tölke, J., Rank, E., 2002. Parallelization strategies and efficiency of CFD computations in complex geometries using Lattice Boltzmann methods on high-performance computers. In: High Performance Scientific and Engineering Computing. Springer, pp. 115–122.

Segars, W., Sturgeon, G., Mendonca, S., Grimes, J., Tsui, B.M., 2010. 4D XCAT phantom for multimodality imaging research. Med. Phys. 37 (9), 4902–4915.

Segars, W., Bond, J., Frush, J., Hon, S., Eckersley, C., Williams, C.H., Feng, J., Tward, D. J., Ratnanather, J., Miller, M., et al., 2013. Population of anatomically variable 4D XCAT adult phantoms for imaging research and optimization. Med. Phys. 40 (4), 043701.

Shadman, R., Criqui, M.H., Bundens, W.P., Fronek, A., Denenberg, J.O., Gamst, A.C., McDermott, M.M., 2004. Subclavian artery stenosis: prevalence, risk factors, and association with cardiovascular diseases. J. Am. Coll. Cardiol. 44 (3), 618–623.

Sherwin, S., Franke, V., Peiró, J., Parker, K., 2003. One-dimensional modelling of a vascular network in space-time variables. J. Eng. Math. 47 (3-4), 217–250.

Tang, C., Zhu, L., Akingba, G., Lu, X.-Y., 2015. Viscous flow past a collapsible channel as a model for self-excited oscillation of blood vessels. J. Biomech. 48 (10), 1922–1929.

Taylor, C.A., Fonte, T.A., Min, J.K., 2013. Computational fluid dynamics applied to cardiac computed tomography for noninvasive quantification of fractional flow reserve. J. Am. Coll. Cardiol. 61 (22), 2233–2241.

Thani, K.B., Kaushal, K., Barnard, D., Copeland, J., Prasad, A., 2011. Coarctation of the thoracic aorta masquerading as bilateral aorto-iliac stenosis. J. Cardiol. Cases 4 (3), e172–e175.

The Visible Human Project, 2015. U.S. National Library of Medicine. https://www.nlm.nih.gov/research/visibl/getting_data.html.

Vergallo, R., Papafaklis, M.I., Yonetsu, T., Bourantas, C.V., Andreou, I., Wang, Z., Fujimoto, J.G., McNulty, I., Lee, H., Biasucci, L.M., et al., 2014. Endothelial shear stress and coronary plaque characteristics in humans. Circ. Cardiovasc. Imaging 7 (6), 905–911.

Warnes, C.A., Williams, R.G., Bashore, T.M., Child, J.S., Connolly, H.M., Dearani, J.A., del Nido, P., Fasules, J.W., Graham, T.P., Hijazi, Z.M., et al., 2008. ACC/AHA 2008 guidelines for the management of adults with congenital heart disease. Circulation 118 (23), e714–e833.

Wilson, N.M., Ortiz, A.K., Johnson, A.B., 2013. The vascular model repository: A public resource of medical imaging data and blood flow simulation results. J. Med. Dev. 7 (4), 040923.

Xiao, N., Humphrey, J.D., Figueroa, C.A., 2013. Multi-scale computational model of three-dimensional hemodynamics within a deformable full-body arterial network. J. Comp. Phys. 244, 22–40.

Xiao, H., Avolio, A., Zhao, M., 2016. Modeling and hemodynamic simulation of human arterial stenosis via tranmission line model. J. Mech. Med. Biol. 16 (05), 1650067.

Xu, D., Li, J., Zou, L., Xu, Y., Hu, D., Pagoto, S.L., Ma, Y., 2010. Sensitivity and specificity of the ankle?brachial index to diagnose peripheral artery disease: a structured review. Vasc. Med. 15 (5), 361–369.

Ziegler, D.P., 1993. Boundary conditions for lattice Boltzmann simulations. J. Stat. Phys. 71 (5-6), 1171–1177.